PLANETARY SCIENCE

From gas to ice giants: A unified mechanism for equatorial jets

Keren Duer-Milner[1,2,3]*, Nimrod Gavriel[1], Eli Galanti[1], Eli Tziperman[4,5], Yohai Kaspi[1]*

The equatorial jets dominating the dynamics of the Jovian planets exhibit two distinct types of zonal flows: strongly eastward in the gas giants (superrotation) and strongly westward in the ice giants (subrotation). Existing theories propose different mechanisms for these patterns, but no single mechanism has successfully explained both. However, the planetary parameters of the four Solar System giant planets suggest that a fundamentally different mechanism is unlikely. In this study, we show that convection-driven columnar structures can account for both eastward and westward equatorial jets, framing the phenomenon as a bifurcation. Consequently, both superrotation and subrotation emerge as stable branches of the same mechanistic solution. Our analysis of these solutions uncovers similarities in the properties of equatorial waves and the leading-order momentum balance. This study suggests that the fundamental dynamics governing equatorial jet formation may be more broadly applicable across the Jovian planets than previously believed, offering a unified explanation for their two distinct zonal wind patterns.

INTRODUCTION

The Jovian planets—Jupiter, Saturn, Uranus, and Neptune—exhibit fascinating atmospheric dynamics, particularly evident in their zonal wind patterns. One of the most distinguishing characteristics among them is the direction of their equatorial jets (1). Jupiter and Saturn exhibit equatorial superrotation, meaning they flow prograde (west to east), in the same direction as the planet's rotation. The term "superrotation" refers to wind velocity that exceeds the angular momentum conserving wind, which is defined using a simple conservation of angular momentum (Eq. 4) (2). Jupiter's jet-stream reaches velocities of ~100 m s^{-1} (3) at the equator, and Saturn, while similar in size and rotation to Jupiter, exhibits a broader and more pronounced equatorial jet, with peak speeds of ~300 m s^{-1} (4, 5) (Fig. 1).

In contrast, Uranus and Neptune have retrograde equatorial jets (east to west), moving opposite to the direction of their rotation (subrotation). The equatorial jet on Uranus reaches wind speeds of ~50 m s^{-1} (6–8) and Neptune's westward jet reaches ~400 m s^{-1} at the equator (9–11). Another notable feature is the presence of alternating midlatitude jets, which are prominent on Jupiter and Saturn, while Uranus and Neptune each have only one jet per hemisphere (Fig. 1). The wind velocity measurements are relative to a uniform rotation rate, which is associated with the planets' interior and aligned with their magnetic field (12). This rotation rate is determined using radio emissions detected by various spacecraft, along with other methodologies [e.g., (5, 13–15)]. Over the past few decades, the jets on all Jovian planets have shown consistency, at least since the advent of modern measurement techniques.

The difference in equatorial jet direction presents a major challenge in planetary science. While it has been suggested in previous studies that the planetary dynamics could be driven by different

mechanisms, it is also possible that they are influenced by similar processes due to their comparable physical characteristics (table S1). All four planets have comparable rotation periods and penetration depths of zonal winds. Jupiter, Saturn, and Neptune also exhibit comparable normalized internal infrared flux. Although Uranus' flux is slightly smaller, its zonal wind structure is remarkably similar to Neptune's, as are their size and mass. The jets on Jupiter penetrate ~0.95 of its radius, according to measured gravity field estimations (16, 17) and ohmic dissipation constraints (18). The jets on Uranus and Neptune penetrate to a maximal depth of ~0.95 (19, 20), meaning they are shallower or equal to the jets on Jupiter (to date, the winds penetration depth of the ice giants has not yet been determined). Saturn's jets reach about 0.84 of its radius (21, 22), indicating a larger proportion related to zonal jets. Other parameters—such as obliquity, where Uranus's is distinct at 98°—vary notably among the planets. However, the considerable differences between Uranus and Neptune are unlikely to be critical in determining the zonal wind mechanisms, as indicated by the similar zonal wind patterns observed on both ice giants. All of this suggests that a common mechanism may be responsible for jet formation and truncation at depth on the Jovian planets.

Theories regarding the formation of zonal jets on giant planets focus on two main mechanisms: convection driven by internal heating [e.g., (23–30)] and baroclinic instability resulting from latitudinal variations in solar radiation [e.g., (31–33)]. Studies using a thin-shell general circulation model have demonstrated that both superrotation and subrotation can occur depending on the energy scheme (34–38). Specifically, solar forcing tends to produce retrograde equatorial jets as baroclinic eddies transport momentum poleward, whereas strong intrinsic heat fluxes leads to prograde equatorial jets due to equatorward momentum convergence by equatorial waves (35). However, these variations may not adequately account for the differences between the planets due to their physical characteristics (table S1). In addition, jets in thin-shell simulations are generally baroclinic and tend to vanish at depths of a few to ~100 bars, although they may penetrate deeper in a different numerical setup (34, 35, 38). This somewhat contradicts recent estimates indicating that Jupiter's and Saturn's jets are relatively

[1]Department of Earth and Planetary Sciences, Weizmann Institute of Science, Rehovot, Israel. [2]Leiden Observatory, Leiden University, Niels Bohrweg 2, 2333 CA, Leiden, Netherlands. [3]SRON Netherlands Institute for Space Research, Niels Bohrweg 4, 2333 CA, Leiden, Netherlands. [4]Department of Earth and Planetary Sciences, Harvard University, Cambridge, MA, USA. [5]School of Engineering and Applied Sciences, Harvard University, Cambridge, MA, USA.
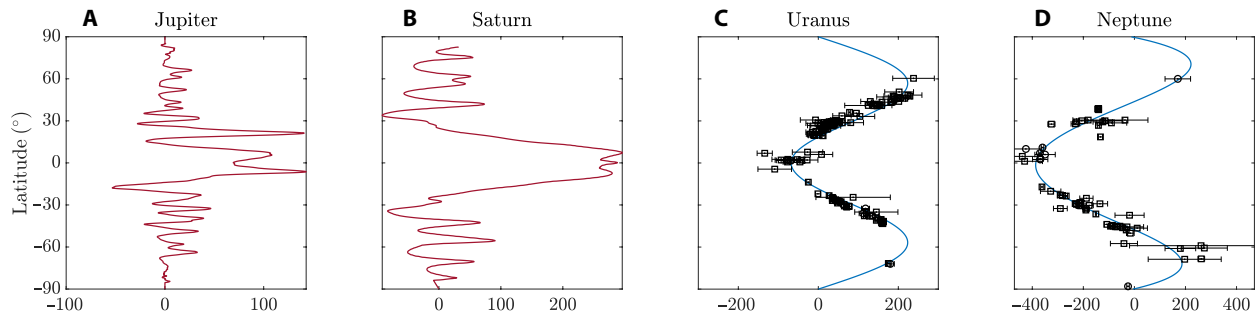*Corresponding author. Email: duer@strw.leidenuniv.nl (K.D.-M.); yohai.kaspi@weizmann.ac.il (Y.K.)

Fig. 1. Measurements of zonal wind profiles of the Jovian planets. Zonally averaged zonal cloud-level winds [m s^{-1}] of (**A**) Jupiter (*3*), (**B**) Saturn (*4*), (**C**) Uranus (*6–8*), and (**D**) Neptune (*10*, *11*). Saturn's wind field incorporates recent estimations of the planet's rotation rate (*5*). The winds on Uranus and Neptune were measured by Voyager 2 (circles) and Hubble Space Telescope (squares) and are presented along with a polynomial fit of the data (line).

barotropic and extend deep (~10^5 bars) into the interior (*16*, *21*, *39*), maintaining a cylindrical orientation along the direction of the axis of rotation (*40*).

Deep, convection-driven three-dimensional (3D) simulations driven by internal heating can also reproduce the banded structure of zonal jets through momentum transport by Reynolds stresses, and laboratory experiments have generally supported these findings (*41*). Studies indicate that the equatorial jets can form in either direction depending on the dominance of Coriolis or buoyancy forces (i.e., Rayleigh number and Ekman number; see Materials and Methods) (*29*, *30*, *42*). While this explanation is effective for understanding different stellar convection model results (the transition between solar and antisolar differential rotation states) (*30*, *43–45*), it may not apply to gas giants. The four Jovian planets exhibit similar rotation rates, with the ice giants rotating ~1.5 times slower than the gas giants. The radii of the ice giants are about one-third those of the gas giants, and with comparable jet speeds, this results in a planetary Rossby number approximately twice as large for the ice giants. However, the Rossby number remains much less than one for all four planets, indicating the continued dominance of rotation in their dynamical state. This suggests that while the transition proposed by (*42*) is plausible, it requires larger Rossby numbers for the ice giants, leaving the underlying mechanisms driving such a transition unclear.

Here, we propose an alternative perspective on the question of equatorial jet direction by using deep convection-driven simulations. Our findings show that a subrotation state can also exist under dominant rotational forces, framing this behavior as a bifurcation with two distinct steady solutions. The formation of the equatorial jet is governed by an equivalent mechanism—tilting columnar convection—highlighting notable similarities in the properties of both solutions. This approach offers an innovative explanation for the distinct equatorial dynamics observed across the Jovian planets.

RESULTS
Theory
Convection-driven equatorial jet formation has been extensively studied and modeled in the past [e.g., (*46*, *47*)]. In simple terms, the convection of heat from the planet's interior outward organizes the flow field, correlating between the components of the anomalous flow (flow velocity that deviates from the averaged value), as long as rotation dominates the momentum balance. This organized columnar convection transfers momentum to the mean zonal wind.

An important aspect of rotating convection is the influence of boundaries that constrain convection cells along the axis of rotation. In the idealized case of a rotating cylindrical annulus, where these boundaries are linear, the circulation within the convective columns (manifested as Reynolds stresses in the momentum balance) facilitates momentum transfer either inward (toward the interior) or outward (toward the outer shell). The direction of this transfer is influenced by the orientation of the columns in the equatorial plane (their tilt), which can develop in either direction (see the equatorial plane cross sections in Fig. 2). This scenario introduces bifurcation, where the tilt can result in two distinct states of mean flow (*48*).

However, when the boundaries are curved, the tilt of the columns is primarily influenced by the curvature of the sloping boundaries. Intuitively, this can be understood as a divergence in the stretching trend: It vanishes in a linear boundary but reverses in its nature between concave and convex boundaries, dictating a variation during the stretching process. Note that, in both scenarios, the columns stretch—commonly referred to as the topographic beta effect. This variation in curvature results in the formation of eastward or westward shear (*49*, *50*), leading to a mean zonal flow that corresponds with the tilt (i.e., superrotating or subrotating jets at the equator). Factors such as the density gradient may contribute to similar opposing behaviors (*51*). The theoretical understanding of this relation between the boundaries and the direction of the convective-driven flow is well established in previous studies [e.g., (*23*)]. However, it has not been explored extensively in numerical studies, possibly due to the unconventional nature of the concave columnar structure.

In spherical geometries as on planets, only positive momentum injection toward the outer shell is sustained due to convex-curvature constraints (Fig. 2, red). In a hypothetical scenario where a convection column does not reach the outer boundary, a reverse tilt can develop, manifesting concave columnar structure, sustaining convection cells, and leading to equatorial subrotation (Fig. 2, blue).

Model formulation
To simulate the equatorial jet of the Jovian planets, we use the open-source, 3D Rayleigh convection model (*52*). The set of equations follow
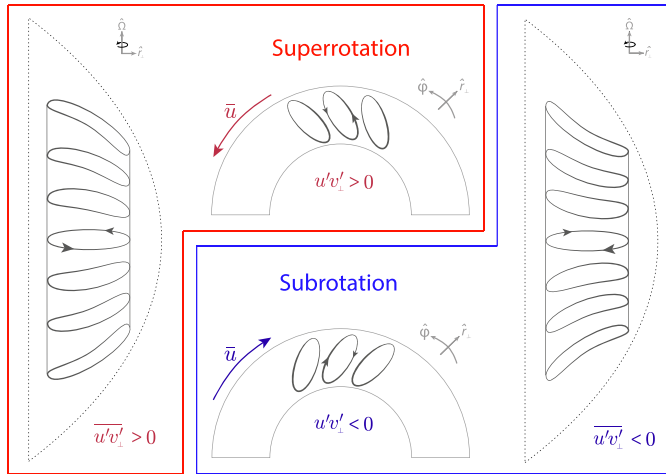
Fig. 2. Schematics of tilted convection columns. The tilt is driving either outward (superrotation, red) or inward (subrotation, blue) transport of positive angular momentum with convex boundaries (dashed envelope). In the subrotation case, the columns have a concave structure while existing within a convex-boundary system. $\hat{\Omega}$ is the direction of the rotation axis, $\hat{r}_\perp$ is the direction perpendicular to the rotation axis, and $\hat{\varphi}$ is the zonal direction. $\bar{u}$ is the mean flow, and $u'v'_\perp$ is the eddy momentum flux directed perpendicular to the rotation axis.

the general formulation used in the hydrodynamics benchmarks [e.g., (53)]. See Materials and Methods for more information.

The momentum equation can be written as

$$\frac{\partial \mathbf{u}}{\partial t} + \mathbf{u} \cdot \nabla \mathbf{u} + 2\mathbf{\Omega} \times \mathbf{u} = \frac{\mathbf{g}S}{C_p} - \nabla\left(\frac{p'}{\bar{\rho}}\right) + \frac{1}{\bar{\rho}}\nabla \cdot \mathbf{D} \qquad (1)$$

where $\bar{\rho}(r)$ is the background-state density, $\mathbf{u}$ is the velocity vector, t is time, $\mathbf{\Omega}$ is the planetary rotation rate, p' is the dynamical pressure, $\mathbf{g}(r)$ is the gravitational acceleration, S is the entropy, and c_p is the specific heat capacity at constant pressure. Last, $\mathbf{D}$ represents the stress tensor.

The zonally averaged zonal momentum equation using Reynolds decomposition for the velocity vector ($\mathbf{u} = \bar{\mathbf{u}} + \mathbf{u}'$, where the bar is the zonal average term and prime denotes deviations from this average, "eddy") gives

$$\frac{\partial \bar{u}}{\partial t} + \bar{\rho}\left(\bar{u} \cdot \nabla\bar{u} + \overline{u' \cdot \nabla u'} - 2\Omega\sin\theta\bar{v} + 2\Omega\cos\theta\bar{w}\right) = F \qquad (2)$$

where the velocity vector $\mathbf{u}$ can be decomposed to u in the zonal direction, v in the meridional direction, and w in the radial direction; θ is the latitude; and F is the viscosity force (see Materials and Methods for full derivation in spherical coordinates). The acceleration of the zonal wind is driven by advection of the mean flow, Reynolds stresses (hereafter referred to as eddy momentum flux $\overline{u'v'}$ and $\overline{u'w'}$) (see Eq. 16), and Coriolis forces, balanced by viscosity. This equation effectively describes the fluid motion that generates equatorial-dominant zonal jets, powered by convection columns oriented parallel to the axis of rotation (29, 54).

Superrotation and subrotation in equivalent conditions
Keeping the physical parameters constant, we explore two cases, starting from rest with random initial entropy noise. The normalized inner radius $\mu = \frac{r_i}{r_o}$ (where the subscripts i and o denote the inner and

outer boundaries, respectively) is set to ~0.92, comparable to the convective envelopes of Jupiter, Uranus, and Neptune. We chose a regime near the onset of rotating convection, namely, the weakly nonlinear regime, where wave properties and force balances can be reliably estimated and resolved. To achieve this, the nondimensional control parameters were set to: $Pr = 3$, $Ek = 7.5 \times 10^{-4}$, and $Ra^* = 0.0132$. It is important to acknowledge that actual planets are expected to exhibit substantialy higher levels of turbulence, conditions that are challenging to achieve in numerical simulations (55). All other parameters controlling the simulations are detailed in the Materials and Methods. In case (a), we observe the well-studied equatorial superrotation driven by convection (Fig. 3A). The right side of the figure shows a snapshot of the zonal wind, illustrating the columnar structure and prograde tilt. The left side presents the zonally averaged zonal wind, confirming the superrotation. In case (b), the scenario is almost a mirror image of case (a) (Fig. 3B). The right side reveals that the zonal wind tilt is oriented in the retrograde direction, while the left side shows the subrotating zonally averaged zonal wind.

As the only difference between the two cases shown in Fig. 3 is the random noise from which the simulations were initiated, it suggests that the problem is essentially a bifurcation problem with two distinct stable solutions. To validate this, we repeated the experiment 10 times and conducted 20 additional experiments at slightly different μ values (~0.91 and 0.93) while keeping other parameters constant (see Materials and Methods and tables S2 and S3). Of the 30 experiments, 15 resulted in subrotation and 15 in superrotation (fig. S4), highlighting the similar likelihood of achieving either solution. However, this distribution is not strictly half and half, but rather reflects a statistical tendency.

Examining the eddy momentum flux terms perpendicular to the axis of rotation ($u'v'_\perp$, which at the equator is equivalent to $u'w'$, Eq. 17) reveals their columnar structure and orientation. In the superrotation case, the columns extend to the spherical boundary of the domain (Fig. 4B) and tilt in the prograde direction ($u'v'_\perp > 0$, pumping momentum outward, Fig. 4C), as predicted by potential vorticity conservation theory—a conserved quantity that combined the effects of circulation, rotation, and stratification (56). In the subrotation case, the columns terminate before reaching the boundary, exhibiting a concave structure (Fig. 4F) and tilt in the retrograde direction ($u'v'_\perp < 0$, pumping momentum inward; Fig. 4G), a phenomenon not previously demonstrated within convex boundaries. The stability of the subrotation and concave columns within the spherical geometry supports the scenario depicted in Fig. 2 (blue).

Examining the full momentum budget (Eqs. 2 and 16) reveals similarities between the two cases in terms of the leading order terms (figs. S1 and S2). In both cases, the Coriolis force terms and eddy momentum flux convergence terms are balanced by the viscosity in the model at steady state. This balance is expected in rotation-dominant convection models [e.g., (28–30, 54, 57)]. In the subrotation case, the columns are truncated before reaching the domain's geometrical boundary, causing the Taylor-Proudman constraint to break near the boundaries, exhibiting a sinusoidal pattern in the cylindrical direction, and revealing vertical variations along the axis of rotation. Theoretical studies often assume that the Taylor-Proudman constraint holds perfectly, which may explain why this solution has not been suggested in the past. In practice, although the Taylor-Proudman constraint is not strictly maintained, the length
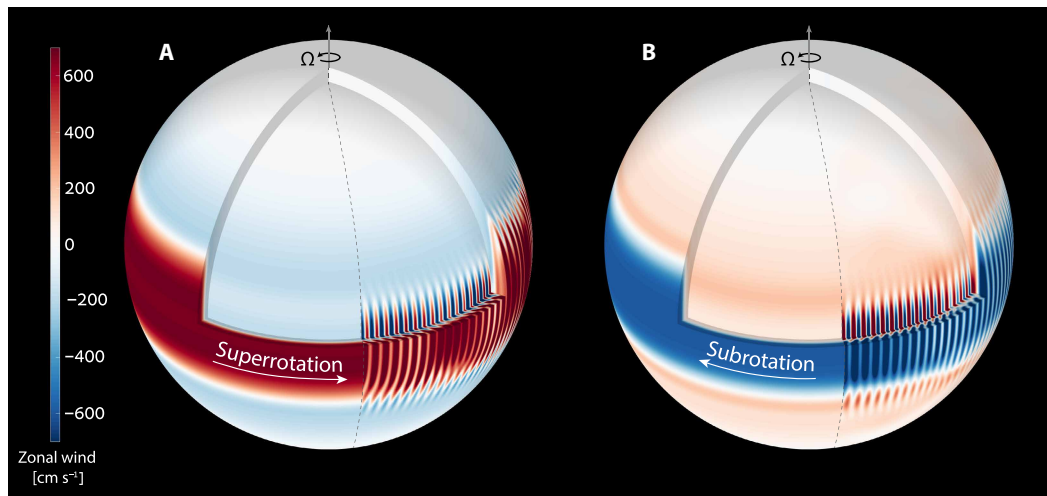
Fig. 3. Results from two simulations with identical physical parameters, initiated from rest with random entropy noise. (**A**) Zonally averaged zonal wind (left side of the sphere) and zonal wind (right side of the sphere) of a convection-driven simulation, showing a superrotating equatorial jet flanked by two retrograde higher-latitude jets. The right side also displays convection columns tilted in the prograde direction. Outer shell is shown for $r = r_o$ and inside the slice values are shown for $r = r_i$ ($\mu = \frac{r_i}{r_o} = 0.92$). (**B**) Similar setup but with reversed patterns: the equatorial jet is subrotating, the higher-latitude jets are in the prograde direction, and the convection columns are tilted in the retrograde direction.
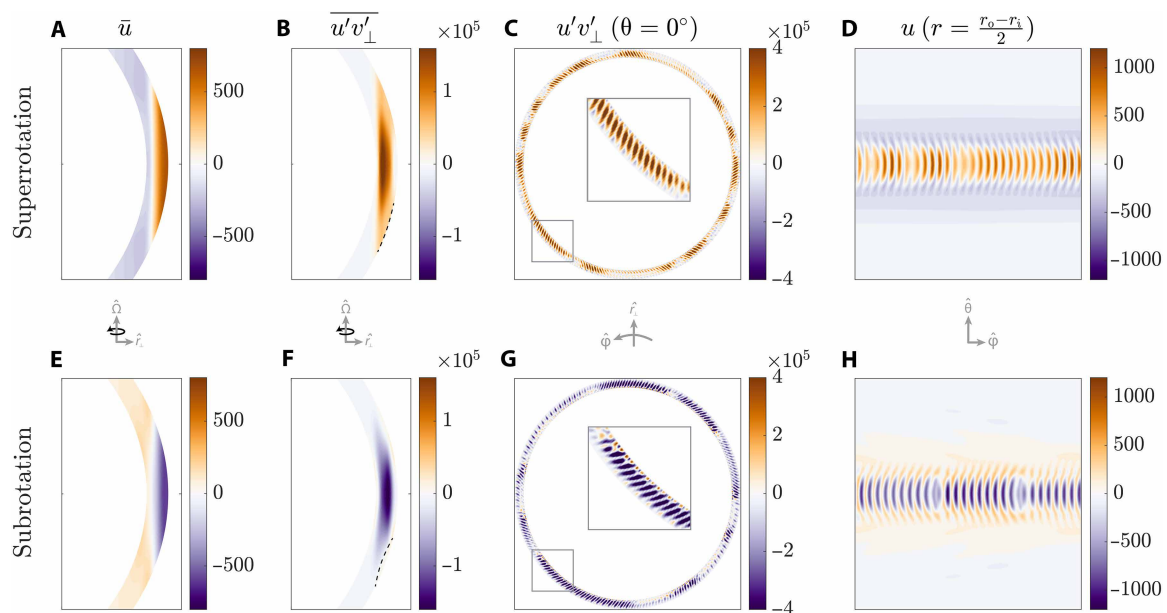

Fig. 4. Zonal wind and eddy fluxes in superrotation and subrotation. Superrotation in the upper panels and subrotation in the bottom panels. (**A** and **E**) Zonally averaged zonal wind [cm s^{-1}] (shown are latitudes $-30°$ to $30°$), (**B** and **F**) Zonally averaged eddy fluxes in the direction perpendicular to the axis of rotation [cm^2 s^{-2}], where the black dashed lines emphasize the curvature of the cylinder at the bottom. (**C** and **G**) Snapshot of eddy fluxes in the equatorial plane [cm^2 s^{-2}], and (**D** and **H**) snapshot of the zonal wind velocity at mid-shell depth [cm s^{-1}]. Both simulations have identical physical parameters and were initiated from random noise. The geometric orientation of the different panels is shown between the upper and lower rows.

scale is still long enough to almost satisfy the Taylor-Proudman theorem, and the flow remains aligned with the rotation axis, indicating that rotation still dominates the momentum balance (*29*).

The onset of the two cases appears identical (fig. S6), with the solutions beginning to drift toward their final steady states after ~30 rotations. Before this point, the outcome remains indeterminate. The analysis of the eddy fluxes at various depths over time (fig. S6, A to C) highlights the temporal variability of the columns, revealing a wave-like structural pattern. At mid-shell depth, a similar analysis shows the temporal and azimuthal propagation of these waves (fig. S6, D and E). In the superrotation case, the waves propagate in the prograde direction, while in the subrotation case, they propagate in the retrograde direction, underscoring the antisymmetry between the two scenarios. Another way to visualize the

wave properties is through a frequency-wave number plot (fig. S7, A and B). The phase speed of the waves can be directly deduced from the trends in these plots, resulting in absolute values of ~1.43 $\pm$ 0.07 m s^{-1} for the superrotating case and 1.40 $\pm$ 0.05 m s^{-1} for the subrotating case (see Materials and Methods and fig. S7). To verify the nature of these waves, we compare the observed values with those of Thermal Rossby waves based on the solutions to the linearized equations that describe convection in a rotating annulus (23, 58). The theoretical value is given by $c_p = -\frac{\beta^*}{k^2}$ (see Materials and Methods), where k is the typical zonal wavenumber (derived from fig. S7, C and D for the calculations, specifically $k_{super} = 2\pi\frac{266}{2\pi R}$ and $k_{sub} = 2\pi\frac{262}{2\pi R}$) and β^* is the topographic beta. At the equator it is $\beta^*(\theta = 0°) = \frac{2\Omega}{H}$ (see Materials and Methods). This yields absolute phase speed values of 1.37 and 1.41 m s^{-1} for superrotation and subrotation, respectively. The alignment between the observed and theoretical values not only reinforces the validity of our numerical results, but also emphasizes the origin and antisymmetry of the equatorial waves that dominate the dynamics.

Bifurcation regime

Next, we focus on examining the regimes of multiple equilibria. Taking the two study cases (Fig. 4), after reaching a dynamical steady state, we vary μ to determine where each solution holds (table S4). We adjust other physical parameters while maintaining the main nondimensional control parameters and the resolution constant (see Materials and Methods and table S2). Starting from the initial conditions shown as dashed horizontal lines in Fig. 5 (red for superrotation, blue for subrotation), 38 simulations were performed (table S4 summarizes the parameters for all the simulations). The resulting steady-state mean zonal wind solutions at the equatorial outer shell are represented by the line and circles. Each simulation runs for 2000 rotations (10 viscous diffusion times, see Materials and Methods), and the final equatorial zonal velocity is presented as the average from the last 100 rotations, along with one SD (Fig. 5, circles).

The figure illustrates a back-to-back saddle-node bifurcation (59, 60), featuring two stable branches. The superrotation branch is the sole stable solution for μ < 0.88, indicative of deep domains. In this regime, the columns are "aware" of the spherical boundaries, resulting in a prograde tilt and a superrotating equatorial jet (orange shade). For mid-values (0.88 < μ < 0.97), both solutions are possible, suggesting that the final outcome is determined by the initial conditions. Here, the columns are likely insensitive to the curvature of the boundaries, allowing for both convex (red shade) and concave (blue shade) columnar structures to exist, or that a competing mechanism balances against the convex boundaries and prevents a preference. In this regime, the relative volume between the cylindrical annulus bounded by the sphere and the curved spherical boundaries is smaller, suggesting a reduced influence of the curved boundaries on the entire column (see the Supplementary Materials). The subrotation branch continues into the regime of 0.97 < μ < 0.99, where it becomes the only stable solution (gray shade). In these relatively shallow domains, the tilt of the columns is likely influenced by an additional mechanism, such as vigorous mixing or potential vorticity stretching [e.g., (29, 42)], inhibiting superrotation. It is also possible that the effective dynamics in this regime exhibit a shallow-layer behavior, resulting in subrotation as commonly observed in models [e.g., (38, 61)]. Notably, as the shell thins, the convective
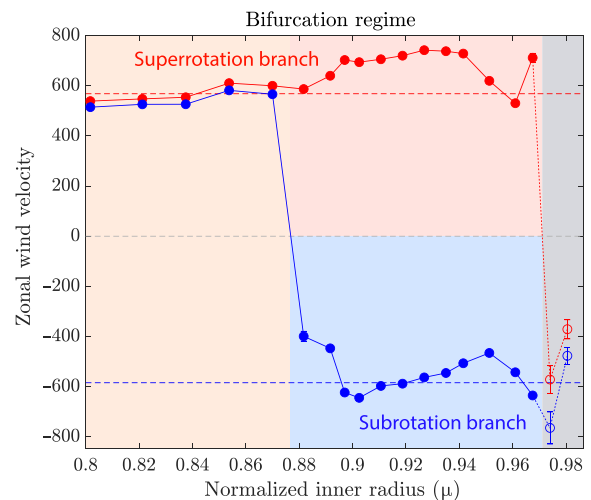

Fig. 5. Thirty-eight simulations revealing a back-to-back saddle-node bifurcation. Two initial conditions are studied: a superrotating case (red dots, with the red dashed line indicating the initial mean velocity value) and a subrotating case (blue dots, with the blue dashed line indicating the initial mean velocity value). For each normalized inner radius ($\mu = \frac{r_i}{r_o}$), two simulations were performed with both sets of initial conditions. All the simulations are in a statistical steady state, with the mean zonal value and error bars, representing one SD, are averaged over the last 100 rotations (mostly notable around the bifurcation nodes, elsewhere the SD is smaller than the circle). The figure reveals four different regions based on μ: A normalized inner radius smaller than μ < 0.88 cannot maintain a concave structure of columns, resulting in a reversion to the superrotation condition (orange shade). Depths in the range (0.88 < μ < 0.97) can support both convex (red shade) and concave (blue shade) columnar structures. Depths associated with μ > 0.97 are presented with open circles and dotted lines as the results are less conclusive (see main text). In this regime (gray shade), only subrotation persists.

structures diminish in size, potentially rendering the resolution too coarse in this thin-shell region. To address this, we use scaling laws to calculate the minimal resolution required to properly resolve the mode at onset (62), ensuring adequate simulation resolution for large normalized inner radii. Therefore, for normalized inner radii larger than μ = 0.95, we repeat the experiment with double the original resolution (fig. S14). The results are generally robust under these changes; however, for very large normalized inner radii (0.97 < μ < 0.99), achieving sustained simulations necessitates an increase in viscosity, leading to reduced velocity values. Consequently, we cannot unequivocally conclude that the subrotation branch is robust in these very shallow domains (μ > 0.97).

Given the estimated wind penetration depth of the Jovian planets, we can deduce their characteristics in relation to the bifurcation shown in Fig. 5. Our results suggest that planets with mid-range convective envelopes may exhibit either state, while very shallow envelopes show only subrotation. In contrast, planets with a deep dynamical layer are likely to exhibit only superrotation. Saturn, with its deep convective envelope (21), falls where only superrotation is a stable branch. In contrast, Jupiter, Uranus, and Neptune lie within regions of two stable solutions (16, 19), indicating that their equatorial jets could potentially orient in either direction. Since the penetration depth of Uranus and Neptune is not yet fully established, it is possible that they could exist in a state where only subrotation is a stable option, which aligns with the observations. Note that the μ values in this figure might not correspond exactly to actual planets,

as the results are model dependent. Moreover, we operate in the weakly nonlinear regime of turbulent convection, an idealized scenario for rotating turbulence. Therefore, while the results shown in Fig. 5 demonstrate the potential for both superrotation and subrotation to occur at large normalized inner radius, further work is needed to directly connect these findings with specific observational constraints (such as the depth of the dynamical region). Last, to ensure the bifurcation is not confined to the specific parameter set used, we conducted a series of sensitivity tests. Our results indicate the bifurcation persists as long as convection organizes into columns (i.e., supercriticality remains above critical) within a similar convective regime (see Materials and Methods). When the model becomes excessively forced (fig. S10), the subrotation branch is no longer sustained. Nonetheless, the bifurcation remains robust within the Boussinesq framework (fig. S13), for slightly less viscous cases (fig. S12), and at higher Pr numbers (fig. S9). These robustness tests suggest that the bifurcation phenomenon we have identified may have broader implications for understanding the dynamics of rotating fluids, extending beyond the specific context of giant planets in the Solar System.

DISCUSSION

This study offers fresh insights into the convective processes driving the emergence of both superrotation and subrotation in fast-rotating spherical shells. By exploring two cases with identical physical parameters starting from random initial noise, we find that both states are achieved once the system reaches a dynamical steady state, suggesting a bifurcation with two stable solutions. This finding is validated by repeated experiments. Eddy flux analysis reveals temporal variability in a wave-like structure, with prograde propagation in superrotation and retrograde propagation in subrotation, highlighting the inherent antisymmetry in these dynamics.

Examining the eddy flux terms reveals their columnar structure and orientation. In the superrotation case, the columns extend to the spherical boundary and tilt in the prograde direction, consistent with theoretical arguments [e.g., (23)]. In the subrotation case, the columns terminate before reaching the boundary, exhibiting a concave structure and retrograde tilt. The full momentum budget analysis shows that in both cases, the Coriolis force and eddy momentum flux convergence are balanced by viscosity at steady state. Despite the Taylor-Proudman constraint breaking near the boundaries in subrotation, rotation, and eddy fluxes remain dominant in the momentum balance, demonstrating the stability of these dynamics within spherical geometry. Frequency–wave number analysis supports our findings, providing phase speeds that align closely with theoretical predictions for Thermal Rossby waves. These insights enhance our understanding of the mechanisms driving superrotation and subrotation and offer a robust framework for future studies in geophysical and astrophysical contexts.

The bifurcating phase space of zonal wind solutions reveals three distinct dynamical regimes. In deep domains, only superrotation is a stable solution, as the spherical boundaries strongly influence the tilt of the convection columns. In the mid-range, both spherical boundaries and mixing could play comparable roles, allowing for either superrotation or subrotation, depending on the initial conditions. In shallow domains, only subrotation is stable, suggesting that the geometrical boundaries lose control over the resulting tilt and zonal wind. In this shallow case, a competing mechanism might play

a role, potentially controlling the direction of the zonal wind shear and subsequently influencing the tilt (reverse causality). For instance, it might exhibit two-dimensional behavior, with potential vorticity mixing around the equator dictating a subrotating equatorial jet and consequently an opposite tilt of the convective columns develops. Note also that the sensitivity of these results to horizontal resolution introduces a degree of uncertainty that warrants careful consideration for very large aspect ratios.

Our results could bear implications for the different flow behaviors observed in the Jovian planets. Saturn fits within the stable superrotation branch, while Jupiter, Uranus, and Neptune lie within the region of two possible stable solutions, suggesting that their equatorial jet formation mechanisms could be equivalent. Due to the lack of clear knowledge on the wind penetration depth on Uranus and Neptune, they might also fall within the solely stable subrotation branch.

Other mechanisms have been proposed to explain the distinctions between gas and ice giants, including the transition from buoyancy-dominated to rotation-dominated dynamics [e.g., (29, 30, 42)], various forcing or dissipation schemes [e.g., (35–37)], notable differences in magnetic fields—particularly the presence of strong nonaxial components in ice giants (63)—and compositional variations that notably affect planetary dynamics (51, 64). While this study introduces a unique unified mechanism to understand the direction of equatorial jets on giant planets, it is important to acknowledge certain limitations. Our simulations focus on a specific, carefully chosen regime near the onset of rotating convection. This regime allows us to isolate and examine the fundamental dynamics responsible for jet formation; however, it does not fully capture the highly turbulent conditions expected in the atmospheres of real planets; these "true" gas giant–like regimes remain numerically unstable in current state-of-the-art 3D rotating convection models (55). Furthermore, although we have examined the robustness of the bifurcation across various parameter changes (see figs. S9 to S14), including more turbulent conditions, a comprehensive exploration of the full parameter space—defined by at least five key dimensions—remains computationally prohibitive.

Despite these constraints, the identification of a bifurcation leading to opposing jet directions and its potential to explain the diverse zonal wind structures observed in gas and ice giants have important implications for understanding atmospheric dynamics of giant planets. The emergence of subrotation from tilted columnar convection has not been previously demonstrated in rotating spherical simulations; in this study, we show that it can arise as a stable solution to the governing equations. We further find that this solution is robust across variations in the normalized inner radius. Our findings underscore the possibility of both superrotation and subrotation arising under identical physical conditions, offering a unified framework to interpret the diverse zonal wind patterns observed on the Jovian planets and shedding light on the fundamental mechanisms behind equatorial jet formation.

MATERIALS AND METHODS
Angular momentum conserving wind

The axial component of specific absolute angular momentum (m) can be defined by

$$m = R\cos\theta \, (\Omega R\cos\theta + u) \tag{3}$$

therefore, the angular momentum-conserving wind of an air parcel at latitude θ that moves poleward from rest at the equator can be expressed as [e.g., (56)]

$$U_\mathrm{m} = \Omega R \frac{\sin^2\theta}{\cos\theta} \quad (4)$$

Since this function varies greatly with latitude, it is clear that only low-latitude winds can be superrotating (2). In particular, if the wind speed at the equator is greater than zero, this indicates a state of superrotation.

Planetary Rossby number

The planetary Rossby number is a dimensionless parameter that measures the relative importance of inertial forces to Coriolis (rotation) forces. At the equator, it is given by

$$Ro = \frac{U}{\Omega R} \quad (5)$$

Since ice giants have similar zonal velocities but rotate at roughly two-thirds the rate of gas giants and have radii about third as large, their Rossby numbers are expected to be approximately twice those of the gas giants.

$$Ro_\mathrm{ice} = \frac{U}{\frac{3}{2}\Omega \times \frac{1}{3}R} = 2Ro_\mathrm{gas} \quad (6)$$

Nonetheless, all four planets have Rossby numbers that are much less than one, indicating that rotation strongly dominates the force balance.

Formulation
Governing equations
The basic equations describing the motion of compressible convection under the anelastic approximation are [following (53, 65)]

$$\frac{\partial \mathbf{u}}{\partial t} - \mathbf{u} \times \boldsymbol{\omega} = -\frac{\nabla p'}{\overline{\rho}} - \nabla \frac{1}{2}\mathbf{u}^2 - 2\boldsymbol{\Omega} \times \mathbf{u} + \mathbf{F}_\nu + \frac{\rho'\mathbf{g}}{\overline{\rho}} \quad (7)$$

$$\nabla \cdot \overline{\rho}\mathbf{u} = 0 \quad (8)$$

$$\frac{p'}{\overline{p}} = \frac{\rho'}{\overline{\rho}} + \frac{T'}{\overline{T}}, \qquad S = \frac{c_\mathrm{p}}{\gamma}\left(\frac{p'}{\overline{p}} - \frac{\gamma\rho'}{\overline{\rho}}\right) \quad (9)$$

$$\overline{\rho}\overline{T}\left(\frac{\partial S}{\partial t} + \mathbf{u} \cdot \nabla S\right) = \nabla \cdot \kappa\overline{\rho}\overline{T}\nabla S + \Pi + Q_\mathrm{i} \quad (10)$$

The equations above are the momentum equation as shown by (66) (Eq. 7), the continuity equation in an anelastic format (Eq. 8), a linearized equation of state, a definition for entropy (Eq. 9), and an evolution equation for entropy (or temperature) (Eq. 10). The thermodynamic variables (p, pressure; T, temperature; and ρ, density) are displayed using Reynolds decomposition, denoted with an overbar for the spatial mean field (reference state) and primes for deviations from this mean state. Here, we take the deviations to be small relative to the reference state. In the momentum equation, $\boldsymbol{\omega} = \nabla \times \mathbf{u}$ is the vorticity and $\mathbf{F}_\nu$ being the viscous force with constant kinematic viscosity ν assuming zero bulk viscosity (no internal

friction) (53). The specific entropy S is defined for perfect gas (67) and $\gamma = \frac{c_\mathrm{p}}{c_\mathrm{v}}$, where c_p is the specific heat capacity at constant pressure and c_v at constant volume. Last, in the entropy equation κ is the turbulent thermal diffusivity, the energy flux is $-\kappa\overline{\rho}\overline{T}\nabla S$ (68), Π is viscous heating, and Q_i is radially dependent internal heating (53). We evolve the equations above in time to solve for the time-dependent variables.

Dimensionless formulation
The hydrodynamic set of equations can be written in a dimensionless form with a set of control parameters. The main three control parameters of the simulations are the modified Rayleigh number $Ra^* = \frac{g_\mathrm{o}\Delta S}{c_\mathrm{p}\Omega^2 L}$ (where the "regular" Rayleigh number is $Ra = \frac{g_\mathrm{o}\Delta S L^3}{\nu\kappa c_\mathrm{p}}$), the Ekman number $Ek = \frac{\nu}{\Omega L^2}$, and the Prandtl number $Pr = \frac{\nu}{\kappa}$ [e.g., (69)], where L is the shell depth, ΔS is the entropy difference across the shell, and g_o is the gravity at the top of the domain. The subscripts i and o denote the inner and outer boundaries, respectively. In addition, we define the dissipation number $Di = \frac{g_\mathrm{o}L}{c_\mathrm{p}T_\mathrm{o}} = \mu\left(e^{\frac{N_\rho}{n}} - 1\right)$, where n is the polytropic index, $N_\rho = ln\left(\frac{\rho_\mathrm{i}}{\rho_\mathrm{o}}\right)$ is the number of density scale heights across the shell, and $\mu = \frac{r_\mathrm{i}}{r_\mathrm{o}}$ is the normalized inner radius (or aspect ratio) (53). Then, the set of equations may be written as (69)

$$\frac{\partial \mathbf{u}}{\partial t} + \mathbf{u} \cdot \nabla\mathbf{u} + 2e_z \times \mathbf{u} = Ra^* \frac{r_\mathrm{o}^2}{r}S\hat{r} - \nabla\left(\frac{p'}{\overline{\rho}}\right) + \frac{Ek}{\overline{\rho}}\nabla \cdot \mathbf{D} \quad (11)$$

$$\overline{\rho}\overline{T}\left(\frac{\partial S}{\partial t} + \mathbf{u} \cdot \nabla S\right) = \frac{Ek}{Pr}\nabla \cdot \overline{\rho}\overline{T}\nabla S + \frac{EkDi}{Ra^*}\Pi + Q_\mathrm{i} \quad (12)$$

$$\mathbf{D} = 2\overline{\rho}\left(e_\mathrm{ij} - \frac{1}{3}\nabla \cdot \mathbf{u}\right), \quad e_\mathrm{ij} = \frac{1}{2}\left(\frac{\partial u_\mathrm{i}}{\partial x_\mathrm{j}} + \frac{\partial u_\mathrm{j}}{\partial x_\mathrm{i}}\right) \quad (13)$$

$$\Pi = 2\overline{\rho}\left[e_\mathrm{ij}e_\mathrm{ji} - \frac{1}{3}(\nabla \cdot \mathbf{u})^2\right] \quad (14)$$

Numerical setup
To analyze equatorial zonal jets in gas giant atmospheres, we use deep convection-driven simulations using the Rayleigh code (52). These simulations can qualitatively replicate the characteristics observed at the outer boundary of the Jovian planets' equatorial regions. We examine the domain depth ($\mu = \frac{r_\mathrm{i}}{r_\mathrm{o}}$ or $L = r_\mathrm{o} - r_\mathrm{i}$) to characterize the bifurcation problem. All simulations in this study employ free-slip velocity boundary conditions, which are suitable for the outer boundary of a gaseous planet and may also represent the inner boundary of the atmosphere, assuming the presence of a fluid interior below [e.g., (53)]. We use fixed entropy boundary conditions at both boundaries, a choice that is straightforward and frequently used in benchmark models [e.g., (53)].

All the simulations use the same control parameters, with Jupiter's radius and rotation rate. Since we use the anelastic dimensional framework, to maintain constant Ek, Ra^*, and Pr values while varying the inner shell depth, we scale the dimensional quantities (the viscosity, thermal diffusivity, and entropy gradient) based on ζ,

where $\zeta = 1 - \frac{7\mu - 2.45}{4.55}$ (tables S2 and S3). This scaling originates from an normalized inner radius (aspect ratio) of $\mu = 0.35$, where $\zeta = 1$. By taking a specific percentage of this shell ($\mu = 0.35$), such as half of it, we achieve $\zeta = 0.5$. The simulations run until they reach a dynamical steady state (1000 to 3000 rotations), equivalent to 5 to 15 viscous diffusion time $\left(t_\nu = \frac{L^2}{\nu}\right)$, with all results showing time-averaged values (excluding snapshots).

The control parameters were chosen within a regime near the onset of rotating convection [i.e., the weakly nonlinear regime (70), the supercriticality of the main experiments (Figs. 3 and 4) is ~5], where the properties of Thermal Rossby waves are distinctly observable, enabling precise quantification and comparison between different solution types. Within this framework, we can properly estimate the fundamental mechanism responsible for equatorial jet formation. Although more turbulent models may more accurately resemble the conditions of real planets, they pose considerable numerical challenges and complicate investigations at large aspect ratios (54). Encompassing the physical parameters of the planets listed in table S1 within the Rayleigh-Ekman-Prandtl parameter space, we observe substantial variations between these parameters and the numerical values used in this study and others (42, 71), largely due to computational limitations. Nonetheless, research suggests that the fundamental physics demonstrated in numerical models can still be applicable to actual physical environments (55).

The zonal momentum equation

Starting from the zonally averaged zonal momentum equation (Eq. 2), considering that the mean momentum fluxes were shown to be small in the ageostrophic order (deviating from the perfect geostrophic balance, the leading order momentum balance as shown in fig. S3) (29, 57, 72), we can write

$$\frac{\partial \overline{u}}{\partial t} + \overline{\rho}\left(\overline{u' \cdot \nabla \mathbf{u}'} - 2\Omega\sin\theta\overline{v} + 2\Omega\cos\theta\overline{w}\right) = \overline{\rho}\nu\nabla^2\overline{u} \quad (15)$$

Using the continuity equation, we can rearrange to write the zonal momentum equation in an anelastic form with spherical coordinates

$$\frac{\partial \overline{u}}{\partial t} + \frac{1}{r^2\cos\theta}\frac{\partial}{\partial \theta}\left(\overline{\rho u'v'}\cos^2\theta\right) + \frac{1}{r^2}\frac{\partial}{\partial r}\left(\overline{\rho u'w'}r^2\cos\theta\right) - \overline{\rho}2\Omega\sin\theta\overline{v}$$
$$+ \overline{\rho}2\Omega\cos\theta\overline{w} = \frac{\overline{\rho}\nu}{r^2\cos\theta}\frac{\partial}{\partial \theta}\left(\cos\theta\frac{\partial \overline{u}}{\partial \theta}\right) + \frac{\overline{\rho}\nu}{r^2}\frac{\partial}{\partial r}\left(r^2\frac{\partial \overline{u}}{\partial r}\right) \quad (16)$$

The eddy momentum flux in the direction perpendicular to the axis of rotation in an anelastic form with spherical coordinates is

$$\frac{\partial \overline{u'v'}_\perp}{\partial r_\perp} = \sin(\theta)\frac{1}{\overline{\rho}r\cos^2\theta}\frac{\partial}{\partial \theta}\left(\overline{\rho u'v'}\cos^2\theta\right)$$
$$+ \cos(\theta)\frac{1}{\overline{\rho}r}\frac{\partial}{\partial r}\left(\overline{\rho u'w'}r\cos\theta\right) \quad (17)$$

At steady state, the primary balance in this equation involves the two Coriolis forces (figs. S1 and S2). When these forces are canceled, the remaining Coriolis terms and the radial eddy momentum flux convergence term are counterbalanced by the radial numerical viscosity (57, 72). Away from the equator, the meridional eddy momentum flux convergence term becomes substantial, contributing more in the direction perpendicular to the axis of rotation (54). This

momentum transfer from the eddy fluxes to the zonal velocity sustains the equatorial zonal wind in both the superrotation and subrotation cases. This primary balance holds for the entire columnar structure outside the tangent cylinder, with contributions from the meridional eddy flux and viscosity terms in the direction perpendicular to the rotation axis. This balance also holds in the mid-latitudes, where solid or parameterized boundaries can represent viscosity (73).

Spectral analysis

To assess the wave-like structure of the columns (visible in Fig. 4, C and D for superrotation and Fig. 4, G and H for subrotation), we conducted a 2D spectral analysis in time and in the zonal direction (fig. S7, A and B), and also averaged over a large time span for generality (between day 300 and day 900, where data are taken every 1 day) (fig. S7 C and D). The frequency spectrum was calculated by taking the two-dimensional (zonal and time dimensions) Fourier transform of the kinetic energy at the equator in the middle of the shell using Matlab's fft2. The time averaging (fig. S7, C and D) reveals three dominant wave numbers at the equator: 1 to 30, representing the mean flow and large-scale patterns; ~260, corresponding to the number of columns; and ~130, representing the half value (fig. S7, C and D). This pattern is evident in Fig. 4 (C and G, insets), where columns appear in front-and-back positions, resulting in a secondary peak at the half value. The difference between the superrotation and subrotation cases is minor; hence, the overall trend remains consistent. Examining the dominant wave number at onset (fig. S6, D and E) reveals that these wave numbers are consistent from onset to dynamical steady state. The phase velocity of the waves apparent in the Hovmöller diagrams (fig. S6, D and E) can be estimated directly from the frequency–wave number spectra by taking the trend of the brightest features in the figure. We performed linear fit to these features by filtering the strongest signals (value > 2×10^6) (see insets in fig. S7, A and B). The resulting values appear in the main manuscript along with one SD of the data. The phase speeds derived from our simulations are valid for the parameters used in our study but should not be interpreted as directly applicable to real planetary conditions, as the simulations are not conducted within the true planetary regime [i.e., Ek and Ra^* numbers are much higher than expectation for real planets (42, 55)].

To assess the theoretical phase speed for these conditions, we begin with Taylor expanding the Coriolis parameter around a latitude θ_0 (56). As the effect of varying the height (topographic beta) is equivalent to the effect of varying the rotation parameter used in meteorology, we use the later for simplicity (23)

$$f = 2\Omega\sin\theta \approx 2\Omega\sin\theta_0 + 2\Omega(\theta - \theta_0)\cos\theta_0 = f_0 + \beta y \quad (18)$$

where $f_0 = 2\Omega\sin\theta_0$, $\beta = \frac{2\Omega\cos\theta_0}{R}$ and $y = R(\theta - \theta_0)$. In the limit of $\theta_0 \to 0$, $\beta y \gg f_0$, hence

$$f_{\theta_0 \to 0} = \beta y = \frac{2\Omega}{R}R\theta \quad (19)$$

This is known as the equatorial beta-plane approximation. Starting from the full dispersion relation found under these conditions (56, 58), we can write

$$\omega^2 - c^2k^2 - \beta\frac{kc^2}{\omega} = (2m+1)\beta c \quad (20)$$

where ω is the dispersion relation, c is the propagation speed, k is the zonal wave number, and $m = 0,1,2 \ldots$. For low-frequency waves, we can neglect terms with ω^2, and the dispersion relation becomes

$$-c^2 k^2 - \beta \frac{kc^2}{\omega} = (2m+1)\beta c \qquad (21)$$

or in a simpler form

$$\omega = \frac{-\beta k}{(2m+1)\beta / c + k^2} \qquad (22)$$

In our case, $k^2 \gg (2m+1)\beta / c$. We further recall the use of the topographic beta instead of the "regular" beta, where $\beta^* = 2\Omega/H$ and H, the scale height, is $H = 0.25R$, corresponding to the height at the center of the cylinder for $\mu = 0.92$. Then, the dispersion relation and phase velocity are

$$\omega = -\frac{\beta^*}{k}, \qquad c_p = -\frac{\beta^*}{k^2} \qquad (23)$$

Variations in the main control parameters

Last, we investigate the sensitivity of the bifurcation behavior to variations in the main control parameters. It is important to recognize that we are operating outside the realm of true physical regimes relevant to the planets, meaning there are no definitive true values for these parameters to compare against. This disconnect underscores the need to examine how variations in these parameters influence the dynamical behavior of the system.

The experiment closely mirrors that described in Fig. 5, where one parameter (e.g., aspect ratio) was varied, while the remaining parameters were held constant at their initial values. The calculation runs were conducted for both super- and subrotation cases, starting from the steady states shown in Figs. 3 and 4. Specifically, the simulations from Figs. 3 and 4 were restarted for an additional 5 or 10 viscous diffusion times, during which one or more parameters were adjusted according to the specific experiment detailed in the Supplementary Materials. We varied four additional control parameters [the Rayleigh number (fig. S10), the Ekman number (fig. S12), the Prandtl number (fig. S9), and the density scale height (fig. S13)], testing both half and double their original values (unless stated otherwise, see Supplementary Text), resulting in 20 additional runs. Furthermore, as higher aspect ratios require high horizontal resolution to properly solve the onset mode (62), we repeat the experiment in Fig. 5 with higher resolution for $\mu > 0.95$ for validity. For aspect ratios $\mu > 0.97$, the Ek had to be increased as well.

In general, operating near the critical value for convection ensures that the bifurcation remains stable, provided that the parameters do not cross critical thresholds. Exceeding these thresholds leads to the breakdown of organized convection (wave patterns), resulting in vigorous mixing [e.g., (42)]. This is evident in several validation tests, including those with low Pr values (fig. S9, bottom row), low Ra values (fig. S10, bottom row), and larger density variations (fig. S13, top row). Moving further into supercriticality yields mixed results: increasing Ra^* leads to the disappearance of the subrotation solution (fig. S10, top row), yet decreasing viscosity by a similar factor allows the bifurcation to persist (fig. S12, middle row), suggesting that the bifurcation's stability is sensitive to the overall parameter combination.

Supplementary Materials

This PDF file includes:
Supplementary Text
Figs. S1 to S14
Tables S1 to S4
References

REFERENCES AND NOTES

1. A. P. Ingersoll, Atmospheric dynamics of the outer planets. *Science* **248**, 308–315 (1990).
2. T. Imamura, J. Mitchell, S. Lebonnois, Y. Kaspi, A. P. Showman, O. Korablev, Superrotation in planetary atmospheres. *Space Sci. Rev.* **216**, 87 (2020).
3. J. Tollefson, M. H. Wong, I. de Pater, A. A. Simon, G. S. Orton, J. H. Rogers, S. K. Atreya, R. G. Cosentino, W. Januszewski, R. Morales-Juberías, P. S. Marcus, Changes in Jupiter's zonal wind profile preceding and during the *Juno* mission. *Icarus* **296**, 163–178 (2017).
4. E. García-Melendo, S. P'érez-Hoyos, A. Sánchez-Lavega, R. Hueso, Saturn's zonal wind profile in 2004–2009 from Cassini ISS images and its long-term variability. *Icarus* **215**, 62–74 (2011).
5. C. R. Mankovich, M. S. Marley, J. J. Fortney, N. Movshovitz, Cassini ring seismology as a probe of Saturn's Interior. I. Rigid Rotation. *Astrophys. J.* **871**, 1 (2019).
6. H. B. Hammel, K. Rages, G. W. Lockwood, E. Karkoschka, I. de Pater, New measurements of the winds of Uranus. *Icarus* **153**, 229–235 (2001).
7. L. A. Sromovsky, P. M. Fry, Dynamics of cloud features on Uranus. *Icarus* **179**, 459–484 (2005).
8. H. B. Hammel, I. de Pater, S. Gibbard, G. W. Lockwood, K. Rages, Uranus in 2003: Zonal winds, banded structure, and discrete features. *Icarus* **175**, 534–545 (2005).
9. B. Conrath, F. M. Flasar, R. Hanel, V. Kunde, W. Maguire, J. Pearl, J. Pirraglia, R. Samuelson, P. Gierasch, A. Weir, B. Bezard, D. Gautier, D. Cruikshank, L. Horn, R. Springer, W. Shaffter, Infrared observations of the Neptunian system. *Science* **246**, 1454–1459 (1989).
10. L. A. Sromovsky, S. S. Limaye, P. M. Fry, Dynamics of Neptune's major cloud features. *Icarus* **105**, 110–141 (1993).
11. L. A. Sromovsky, P. M. Fry, T. E. Dowling, K. H. Baines, S. S. Limaye, Neptune's atmospheric circulation and cloud morphology: Changes revealed by 1998 HST imaging. *Icarus* **150**, 244–260 (2001).
12. M. D. Desch, M. L. Kaiser, Voyager measurement of the rotation period of Saturn's magnetic field. *Geophys. Res. Lett.* **8**, 253–256 (1981).
13. R. Helled, G. Schubert, J. D. Anderson, Jupiter and Saturn rotation periods. *Planet. Space Sci.* **57**, 1467–1473 (2009).
14. R. Helled, J. D. Anderson, G. Schubert, Uranus and Neptune: Shape and rotation. *Icarus* **210**, 446–454 (2010).
15. R. Helled, E. Galanti, Y. Kaspi, Saturn's fast spin determined from its gravitational field and oblateness. *Nature* **520**, 202–204 (2015).
16. Y. Kaspi, E. Galanti, W. B. Hubbard, D. J. Stevenson, S. J. Bolton, L. Iess, T. Guillot, J. Bloxham, J. E. P. Connerney, H. Cao, D. Durante, W. M. Folkner, R. Helled, A. P. Ingersoll, S. M. Levin, J. I. Lunine, Y. Miguel, B. Militzer, M. Parisi, S. M. Wahl, Jupiter's atmospheric jet streams extend thousands of kilometres deep. *Nature* **555**, 223–226 (2018).
17. K. Duer, E. Galanti, Y. Kaspi, The range of Jupiter's flow structures that fit the Juno asymmetric gravity measurements. *J. Geophys. Res. Planets* **125**, e2019JE006292 (2020).
18. J. Liu, P. M. Goldreich, D. J. Stevenson, Constraints on deep-seated zonal winds inside Jupiter and Saturn. *Icarus* **196**, 653–664 (2008).
19. Y. Kaspi, A. P. Showman, W. B. Hubbard, O. Aharonson, R. Helled, Atmospheric confinement of jet streams on Uranus and Neptune. *Nature* **497**, 344–347 (2013).
20. D. Soyuer, F. Soubiran, R. Helled, Constraining the depth of the winds on Uranus and Neptune via Ohmic dissipation. *Mon. Not. R. Astron. Soc.* **498**, 621–638 (2020).
21. E. Galanti, Y. Kaspi, Y. Miguel, T. Guillot, D. Durante, P. Racioppa, L. Iess, Saturn's deep atmospheric flows revealed by the Cassini grand finale gravity measurements. *Geophys. Res. Lett.* **46**, 616–624 (2019).
22. Y. Kaspi, E. Galanti, A. P. Showman, D. J. Stevenson, T. Guillot, L. Iess, S. J. Bolton, Comparison of the deep atmospheric dynamics of Jupiter and Saturn in light of the Juno and Cassini gravity measurements. *Space Sci. Rev.* **216**, 1–27 (2020).
23. F. H. Busse, Convection driven zonal flows and vortices in the major planets. *Chaos* **4**, 123–134 (1994).
24. U. R. Christensen, Zonal flow driven by deep convection in the major planets. *Geophys. Res. Lett.* **28**, 2553–2556 (2001).
25. J. M. Aurnou, P. L. Olson, Strong zonal winds from thermal convection in a rotating spherical shell. *Geophys. Res. Lett.* **28**, 2557–2559 (2001).
26. M. Heimpel, J. Aurnou, J. Wicht, Simulation of equatorial and high-latitude jets on Jupiter in a deep convection model. *Nature* **438**, 193–196 (2005).
27. Y. Kaspi, G. R. Flierl, Formation of jets by baroclinic instability on gas planet atmospheres. *J. Atmos. Sci.* **64**, 3177–3194 (2007).
28. C. A. Jones, K. M. Kuzanyan, Compressible convection in the deep atmospheres of giant planets. *Icarus* **204**, 227–238 (2009).

29. Y. Kaspi, G. R. Flierl, A. P. Showman, The deep wind structure of the giant planets: Results from an anelastic general circulation model. *Icarus* **202**, 525–542 (2009).

30. T. Gastine, J. Wicht, J. M. Aurnou, Zonal flow regimes in rotating anelastic spherical shells: An application to giant planets. *Icarus* **225**, 156–172 (2013).

31. G. P. Williams, Planetary circulations: 1. Barotropic representation of Jovian and terrestrial turbulence. *J. Atmos. Sci.* **35**, 1399–1426 (1978).

32. J. Y.-K. Cho, L. M. Polvani, The morphogenesis of bands and zonal winds in the atmospheres on the giant outer planets. *Science* **273**, 335–337 (1996).

33. J. Y.-K. Cho, L. M. Polvani, The emergence of jets and vortices in freely evolving, shallow-water turbulence on a sphere. *Phys. Fluids* **8**, 1531–1552 (1996).

34. T. Schneider, J. Liu, Formation of jets and equatorial superrotation on Jupiter. *J. Atmos. Sci.* **66**, 579–601 (2009).

35. J. Liu, T. Schneider, Mechanisms of jet formation on the giant planets. *J. Atmos. Sci.* **67**, 3652–3672 (2010).

36. R. M. B. Young, P. L. Read, Y. Wang, Simulating Jupiter's weather layer. Part I: Jet spin-up in a dry atmosphere. *Icarus* **326**, 225–252 (2019).

37. Y. Lian, A. P. Showman, Deep jets on gas-giant planets. *Icarus* **194**, 597–615 (2008).

38. I. Guendelman, Y. Kaspi, An idealized general circulation model for the atmospheric circulation on the Ice Giants. arXiv:2509.17217 [Preprint] (2025).

39. E. Galanti, Y. Kaspi, Combined magnetic and gravity measurements probe the deep zonal flows of the gas giants. *Mon. Not. R. Astron. Soc.* **501**, 2352–2362 (2021).

40. Y. Kaspi, E. Galanti, R. S. Park, K. Duer, N. Gavriel, D. Durante, L. Less, M. Parisi, D. R. Buccino, T. Guillot, D. J. Stevenson, S. J. Bolton, Observational evidence for cylindrically oriented zonal flows on Jupiter. *Nat. Astron.* **7**, 1463–1472 (2023).

41. D. Lemasquerier, B. Favier, M. Le Bars, Zonal jets at the laboratory scale: Hysteresis and Rossby waves resonance. *J. Fluid Mech.* **910**, A18 (2021).

42. J. Aurnou, M. Heimpel, J. Wicht, The effects of vigorous mixing in a convective model of zonal flow on the ice giants. *Icarus* **190**, 110–126 (2007).

43. N. A. Featherstone, B. W. Hindman, The spectral amplitude of stellar convection and its scaling in the high-Rayleigh-number regime. *Astrophys. J.* **818**, 32 (2016).

44. B. W. Hindman, N. A. Featherstone, K. Julien, Morphological classification of the convective regimes in rotating stars. *Astrophys. J.* **898**, 120 (2020).

45. M. E. Camisassa, N. A. Featherstone, Solar-like to antisolar differential rotation: A geometric interpretation. *Astrophys. J.* **938**, 65 (2022).

46. F. H. Busse, A simple model of convection in the Jovian atmosphere. *Icarus* **29**, 255–260 (1976).

47. F. H. Busse, Asymptotic theory of convection in a rotating, cylindrical annulus. *J. Fluid Mech.* **173**, 545–556 (1986).

48. L. N. Howard, R. Krishnamurti, Large-scale flow in turbulent convection: A mathematical model. *J. Fluid Mech.* **170**, 385–410 (1986).

49. F. H. Busse, L. L. Hood, Differential rotation driven by convection in a rapidly rotating annulus. *Geophys. Astrophys. Fluid Dyn.* **21**, 59–74 (1982).

50. K. Zhang, Spiralling columnar convection in rapidly rotating spherical fluid shells. *J. Fluid Mech.* **236**, 535–556 (1992).

51. G. Glatzmaier, M. Evonuk, T. Rogers, Differential rotation in giant planets maintained by density-stratified turbulent convection. *Geophys. Astrophys. Fluid Dyn.* **103**, 31–51 (2009).

52. N. A. Featherstone, P. V. Edelmann, R. Gassmoeller, L. I. Matilsky, R. J. Orvedhal, C. R. Wilson, geodynamics/Rayleigh: Rayleigh Version 1.1.0 (1.1.0). (Zenodo, 2022).

53. C. A. Jones, P. Boronski, A. S. Brun, G. A. Glatzmaier, T. Gastine, M. S. Miesch, J. Wicht, Anelastic convection-driven dynamo benchmarks. *Icarus* **216**, 120–135 (2011).

54. K. Duer, E. Galanti, Y. Kaspi, Depth dependent dynamics explain the equatorial jet difference between Jupiter and Saturn. *Geophys. Res. Lett.* **51**, e2023GL107354 (2024).

55. A. P. Showman, Y. Kaspi, G. R. Flierl, Scaling laws for convection and jet speeds in the giant planets. *Icarus* **211**, 1258–1273 (2011).

56. G. K. Vallis, *Atmospheric and Oceanic Fluid Dynamics* (Cambridge Univ. Press, ed. 2, 2017), p. 770.

57. K. Duer, E. Galanti, Y. Kaspi, Gas giant simulations of eddy-driven jets accompanied by deep meridional circulation. *AGU Adv.* **4**, e2023AV000908 (2023).

58. B. W. Hindman, R. Jain, Radial trapping of thermal Rossby waves within the convection zones of low-mass stars. *Astrophys. J.* **932**, 68 (2022).

59. S. H. Strogatz, *Nonlinear Dynamics and Chaos: With Applications to Physics, Biology, Chemistry and Engineering* (Addison-Wesley Publishing Company, 1994).

60. H. A. Dijkstra, Numerical bifurcation methods applied to climate models: Analysis beyond simulation. *Nonlinear Processes Geophys.* **26**, 359–369 (2019).

61. R. Chemke, Y. Kaspi, Poleward migration of eddy driven jets. *J. Adv. Model. Earth Syst.* **7**, 1457–1471 (2015).

62. A. Barik, S. A. Triana, M. Calkins, S. Stanley, J. Aurnou, Onset of convection in rotating spherical shells: Variations with radius ratio. *Earth Space Sci.* **10**, e2022EA002606 (2023).

63. K. M. Soderlund, S. Stanley, The underexplored frontier of ice giant dynamos. *Philos. Trans. R. Soc. Lond. A* **378**, 20190479 (2020).

64. T. Guillot, L. N. Fletcher, R. Helled, M. Ikoma, M. R. Line, V. Parmentier, Giant Planets from the Inside-Out. arXiv:2205.04100 [astro-ph.EP] (2022).

65. W. Dietrich, C. A. Jones, Anelastic spherical dynamos with radially variable electrical conductivity. *Icarus* **305**, 15–32 (2018).

66. S. Chandrasekhar, *Hydrodynamic and hydromagnetic stability* (Dover Publications Inc., 1961).

67. L. D. Landau, E. M. Lifshitz, *Fluid Mechanics* (Pergamon Press, 1959), vol. 6.

68. S. I. Braginsky, P. H. Roberts, Equations governing convection in Earth's core and the geodynamo. *Geophys. Astrophys. Fluid Dyn.* **79**, 1–97 (1995).

69. M. Heimpel, T. Gastine, J. Wicht, Simulation of deep-seated zonal jets and shallow vortices in gas giant atmospheres. *Nat. Geosci.* **9**, 19–23 (2016).

70. T. Gastine, J. Wicht, J. Aubert, Scaling regimes in spherical shell rotating convection. *J. Fluid Mech.* **808**, 690–732 (2016).

71. U. R. Christensen, Zonal flow driven by strongly supercritical convection in rotating spherical shells. *J. Fluid Mech.* **470**, 115–133 (2002).

72. Y. Kaspi, Turbulent convection in rotating anelastic spheres: A model for the circulation on the giant planets. Massachusetts Institute of Technology (2008).

73. K. Duer, N. Gavriel, E. Galanti, Y. Kaspi, L. N. Fletcher, T. Guillot, S. J. Bolton, S. M. Levin, S. K. Atreya, D. Grassi, A. P. Ingersoll, L. Cheng, L. Liming, J. I. Lunine, G. Orton, F. A. Oyafuso, J. H. Waite, Evidence for multiple Ferrel-like cells on Jupiter. *Geophys. Res. Lett.* **48**, e2021GL095651 (2021).

74. A. P. Ingersoll, D. Banfield, The energy balance of the giant planets. *Science* **262**, 1842–1846 (1993).

75. J. C. Pearl, B. J. Conrath, R. A. Hanel, J. A. Pirraglia, A. Coustenis, The albedo, effective temperature, and energy balance of Uranus, as determined from Voyager IRIS data. *Icarus* **84**, 12–28 (1990).

76. W. B. Hubbard, W. J. Nellis, A. C. Mitchell, N. C. Holmes, P. C. McCandless, S. S. Limaye, Interior structure of Neptune—Comparison with Uranus. *Science* **253**, 648–651 (1991).

77. J. C. Pearl, B. J. Conrath, The albedo, effective temperature, and energy balance of Neptune, as determined from Voyager data. *J. Geophys. Res.* **96**, 18921–18930 (1991).

78. T. Guillot, A comparison of the interiors of Jupiter and Saturn. *Planet. Space Sci.* **47**, 1183–1200 (1999).

79. L. Li, B. J. Conrath, P. J. Gierasch, R. K. Achterberg, C. A. Nixon, A. A. Simon-Miller, F. M. Flasar, D. Banfield, K. H. Baines, A. P. Ingersoll, A. R. Vasavada, A. D. Del Genio, C. C. Porco, A. A. Mamoutkine, M. E. Segura, G. L. Bjoraker, G. S. Orton, L. N. Fletcher, P. G. J. Irwin, P. L. Read, Saturn's emitted power. *J. Geophys. Res. Planets* **115**, E11002 (2010).

80. L. Li, X. Jiang, R. A. West, P. J. Gierasch, S. Perez-Hoyos, A. Sanchez-Lavega, L. N. Fletcher, J. J. Fortney, B. Knowles, C. C. Porco, K. H. Baines, P. M. Fry, A. Mallama, R. K. Achterberg, A. A. Simon, C. A. Nixon, G. S. Orton, U. A. Dyudina, S. P. Ewald, R. W. Schmude Jr., Less absorbed solar energy and more internal heat for Jupiter. *Nat. Commun.* **9**, 3709 (2018).

81. Y. Kaspi, Inferring the depth of the zonal jets on Jupiter and Saturn from odd gravity harmonics. *Geophys. Res. Lett.* **40**, 676–680 (2013).

82. J. M. Martins, L. A. Sromovsky, P. M. Fry, Thermal emission of the giant planets from Cassini and Voyager measurements. *Icarus* **219**, 277–289 (2012).

83. R. Hanel, B. Conrath, P. Gierasch, P. Song, M. Kaiser, T. Magorrian, Thermal emission spectra of the Jovian and saturnian atmospheres from voyager IRIS measurements. *J. Geophys. Res.* **86**, 10637–10660 (1981).

84. G. Milcareck, S. Guerlet, F. Montmessin, A. Spiga, J. Leconte, E. Millour, N. Clement, L. N. Fletcher, M. T. Roman, E. Lellouch, R. Moreno, Radiative-convective models of the atmospheres of Uranus and Neptune: heating sources and seasonal effects. *Astron. Astrophys.* **686**, A303 (2024).

Supplementary Materials. The numerical results discussed in this study were derived by applying the Rayleigh convection model to solve the hydrodynamic equations. For a detailed overview of the methodology, please refer to (*52*). In this context, we used a specific set of parameters and a defined reference state, which are elaborated in the main text and further detailed in the Supplementary Materials. This approach allowed us to simulate the dynamics of the planetary systems and analyze the resulting behavior under the specified conditions. The choice of parameters and reference state is critical, as they strongly influence the outcomes and interpretations of the simulations. See Materials and Methods for further details and discussion.